Chemical Engineering Journal 361 (2019) 1296–1303

Contents lists available at ScienceDirect

Chemical Engineering Journal

journal homepage: www.elsevier.com/locate/cej

Rationally assembled porous carbon superstructures for advanced supercapacitors

Bingni Gu[a], Hai Su[a], Xiang Chu[a], Qing Wang[a], Haichao Huang[a], Jiaqi He[a], Taojian Wu[a], Weili Deng[a], Haitao Zhang[a,*], Weiqing Yang[a,b,*]

[a] *Key Laboratory of Advanced Technologies of Materials (Ministry of Education), School of Materials Science and Engineering, Southwest Jiaotong University, Chengdu 610031, China*

[b] *State Key Laboratory of Traction Power, Southwest Jiaotong University, Chengdu 610031, China*

HIGHLIGHTS

- RCSSs are rationally synthesized by in-situ conversion with ex-situ assembly method.
- RCSSs exhibit excellent rate capability and cycle stability.
- High-power density and high energy density are simultaneously achieved.

GRAPHICAL ABSTRACT

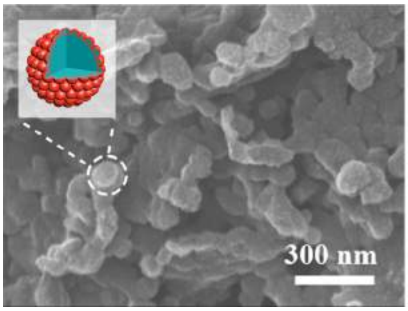

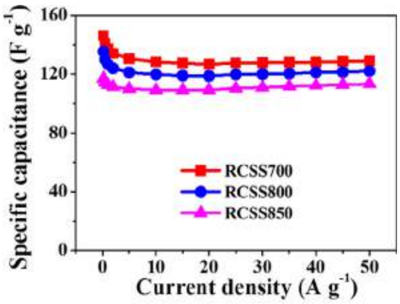

ARTICLE INFO

Keywords:
Bottom-up method
Carbon superstructures
Supercapacitors
High-power density
Long cycle life

ABSTRACT

Rationally designing three-dimensional complex carbon superstructures for energy storage applications offers opportunities to tackle challenges driven by increasingly higher demand of portable energy devices. Herein we report in-situ controlled constructibility and ex-situ confined assembly strategies to enable novel raspberry-like carbon superstructures (RCSSs) for the enhancement of advanced supercapacitors. Through precise control of edge-to-surface ratio and optimization of inner pore structure, the resultant RCSSs show three-dimensional hierarchical porous framework, large specific surface area (SSA, ~1000 $m^2 g^{-1}$) and high electrical conductivity (~2700 $S m^{-1}$), which facilitate ion diffusion and electron transfer. The predesigned RCSSs used as the electrode materials in symmetrical supercapacitors exhibit high rate capability, as indicated by 25,000% increment of the current density only leading to low capacitance degradation of 11.7%, and show long-term cycling stability (98.3% retention after 10,000 cycles) in 6 M KOH electrolyte. Moreover, the RCSSs simultaneously deliver high energy density of 46.5 $Wh kg^{-1}$ and high power density of 52.5 $kW kg^{-1}$ in ionic liquid electrolytes. We believe that the combination of in-situ and ex-situ approaches yielded carbon superstructures with complex microstructure and outstanding electrical properties show promising application for universally advanced energy devices with superior power and energy characteristics.

---

* Corresponding authors at: Key Laboratory of Advanced Technologies of Materials (Ministry of Education), School of Materials Science and Engineering, Southwest Jiaotong University, Chengdu 610031, China (W. Yang).

E-mail addresses: haitaozhang@swjtu.edu.cn (H. Zhang), wqyang@swjtu.edu.cn (W. Yang).

https://doi.org/10.1016/j.cej.2019.01.007
Received 2 September 2018; Received in revised form 27 December 2018; Accepted 2 January 2019

1. Introduction

Supercapacitors, as a new type of electrochemical energy-storage devices, have been widely used in uninterruptible power supplies, high power electronic devices, renewable integration and hybrid electric vehicles due to the advantages of high power density, long cycle life and fast charging/discharging rate [1–5]. Carbon materials, such as nanotubes, graphene, activated carbon, carbide derived carbon, are considered as ideal electrode materials for electric double-layer capacitors (EDLCs) since their large specific surface area, adjustable pore structure, and unique electronic structure. And the microstructures of carbon materials have been proved to play an important role on EDL capacitive performance [6–10]. Suitable carbon structure by rational design will promote the utilization of the pore channels and enhance the accessible surface area, and thus to realize improved electrochemical properties. The increasing demand of high-performance supercapacitors has attracted enormous research efforts on the top-level design and precise control of complex three-dimensional carbon structures [11–13]. Among the various carbon materials, carbon superstructures consisting of mesoscopic or macroscopic architectures show tunable morphologies and structures for energy storage.

The last ten years have witnessed some breakthroughs on designing carbon superstructures [14–17]. Graphene superstructures, as one typical complex carbon superstructures, show exceptional properties inherited from graphene layers and superior electrical properties. Such graphene-based superstructures can be prepared by controlling the organization process of the functionalized graphene materials that were synthesized from top-down method like exfoliation of graphite. However, this method towards graphene superstructures is blocked by multiple steps including complex chemical oxidation/reduction and reassembling process [18–21]. As electrode materials in supercapacitors, these graphene superstructures suffer from low power density and severe self-discharge effect [22–24]. Hence, resorting to novel methods to produce complex but highly ordered carbon superstructures is still a matter of general interest but great challenge.

Alternatively, bottom-up method can achieve what other methods such as the bottom-up surface-mediated synthesis or top-down strategy cannot achieve, which gives an alternative choice for precise control of carbon superstructures. Recently, carbon superstructures constructed by nanosheets have been successfully synthesized through controlling the geometric parameter of the carbon layers and structurally defined growth [17,25–27]. However, progresses for complex carbon structures have been explored partially and mainly focus on the potential applications to meet particular requirement. For this reason, exploitation of novel methods to process carbon superstructures such as low dimensional segment self-assembly and its related applications require further investigation.

Conversion of CO_2 into functional carbonaceous materials, as a typical bottom-up method, is of great significance because the most abundant CO_2 greenhouse gas is responsible to global warming. Although enormous research efforts have been devoted to the photocatalytic, hydrogenation or electrocatalyst reduction of CO_2 into hydrocarbon fuels like methane (CH_4) [28–31] or methanol (CH_3OH) [32–34], there are just a few strategies have been proposed to convert CO_2 into solid carbonaceous materials. For example, Wei et al. fabricated cauliflower-fungus-like graphene through the reaction between CO_2 gas and Li liquid [35]. Xing et al. reduced CO_2 to dense nanoporous graphene, in which Mg acted as the reductant and Zn contributed to enhanced nanoporosity [36]. And our previous work indicated that the resultant nanocarbons could be fine-tuned through controlling the interfacial reaction between CO_2 and Mg [37]. However, studies on directly converting CO_2 into well-ordered complex carbonaceous superstructures that is of widespread interest for functional materials with enhanced properties have not been exploited.

Herein, we design novel carbon superstructures by in-situ conversion and ex-situ assembly methods through which carbon layers generate and simultaneously self-assemble on MgO confined templates. Reactive metal Mg acts as a reducing agent in this facile MgO template method and CO_2 is converted into three-dimensional carbonaceous material with interconnected porous structure. It is novel that the conversion of CO_2 cooperates with template method to produce well-ordered carbonaceous structures composed of nanoparticles less than 10 nm in size. Such a complex three-dimensional carbon structure is named as superstructure. The rationally designed raspberry-like carbon superstructures exhibit well-organized porous structure, large surface area, and high electrical conductivity. As expected, the symmetric supercapacitors based on RCSSs display impressive electrochemical performance. Besides good rate performance and long-term cycling stability, the supercapacitors deliver high energy density and high power density.

2. Experimental

2.1. Preparation and microstructural characterizations of RCSSs

To prepare RCSSs, the first step was to mix the particle-like MgO with Mg powder at a mass ratio of 1:6 ~ 6:1 through ball-milling technique. Then, 3 g mixture was spread in a corundum boat and then put into a tubular furnace (GSL-1700X, Hefei Kejing Materials Tech. Co., Ltd., China). After flushed with an Ar flow of 200 sccm for 30 min, the tube was heated to the aimed reaction temperature (600–900 °C) at a heating rate of $4\,^{\circ}C\,min^{-1}$ under Ar atmosphere and kept for 2 h with a CO_2 flow of 20 sccm. Similar fabrications via the reaction between Mg and CO_2 have been reported before [36–38]. After conversion, the resultants were treated with enough 1 M HCl to dissolve the MgO impurities and then washed with deionized water. According to the aimed reaction temperature, the obtained samples were denoted as RCSS600, RCSS650, RCSS700, RCSS800, RCSS850, and RCSS900. Since the samples prepared at the temperature lower than 650 °C or above 900 °C are quite few due to the melted or vaporized unreacted Mg, we mainly focus on analyzing the morphology and electrochemical properties of RCSS700, RCSS800, and RCSS850 samples.

Scanning electron microscopy (SEM) measurements were carried out on the JEOL JSM–7800 Prime with an accelerating voltage of 5 kV. Transmission electron microscopy (TEM) and high-resolution TEM (HRTEM) detections were measured by the ZEISS Libra 200 FE. X-ray diffraction (XRD) data were recorded using a PANalytical X'Pert powder diffractometer with a Cu kα source. Raman spectra were tested by RM2000 microscopic confocal Raman spectrometer employing a 514 nm laser beam. X-ray photoelectron spectroscopy (XPS) measurements were performed on Thermo Scientific ESCALAB 250Xi. Micromeritics ASAP 2020 surface area and pore size analyzer was used to get N_2 adsorption–desorption isotherms of the RCSSs at –196 °C. The Brunauer-Emmertt-Teller (BET) surface areas and the pore size distribution (PSD) were analyzed according to the Barrett-Joyner-Halenda (BJH) method and the density functional theory (DFT) method. The electrical conductivities of the RCSSs were determined using a four-probe technique (RTS9, China). For conductivity measurement, the as-prepared RCSSs were compacted into round pieces of 13 mm in diameter and 0.5 mm in thickness under pressure of 10 MPa. Each sample was measured in three regions and the results were averaged. The contact angle of the as-prepared RCSS-based electrode films was tested on a Dataphysics DSA100 contact-angle system at room temperature.

2.2. Preparation and electrochemical measurements of RCSS-based supercapacitors

The supercapacitor electrode materials consisting of RCSSs, PTFE (Sigma-Aldrich), and conductive additive (Super C45, Timical) with a mass ratio of 85:10:5 were homogeneously mixed, blended, fully kneaded and rolled into the sheets with a thickness of 100 μm. To assemble CR2032 coin-type cells, a polypropylene paper separator was

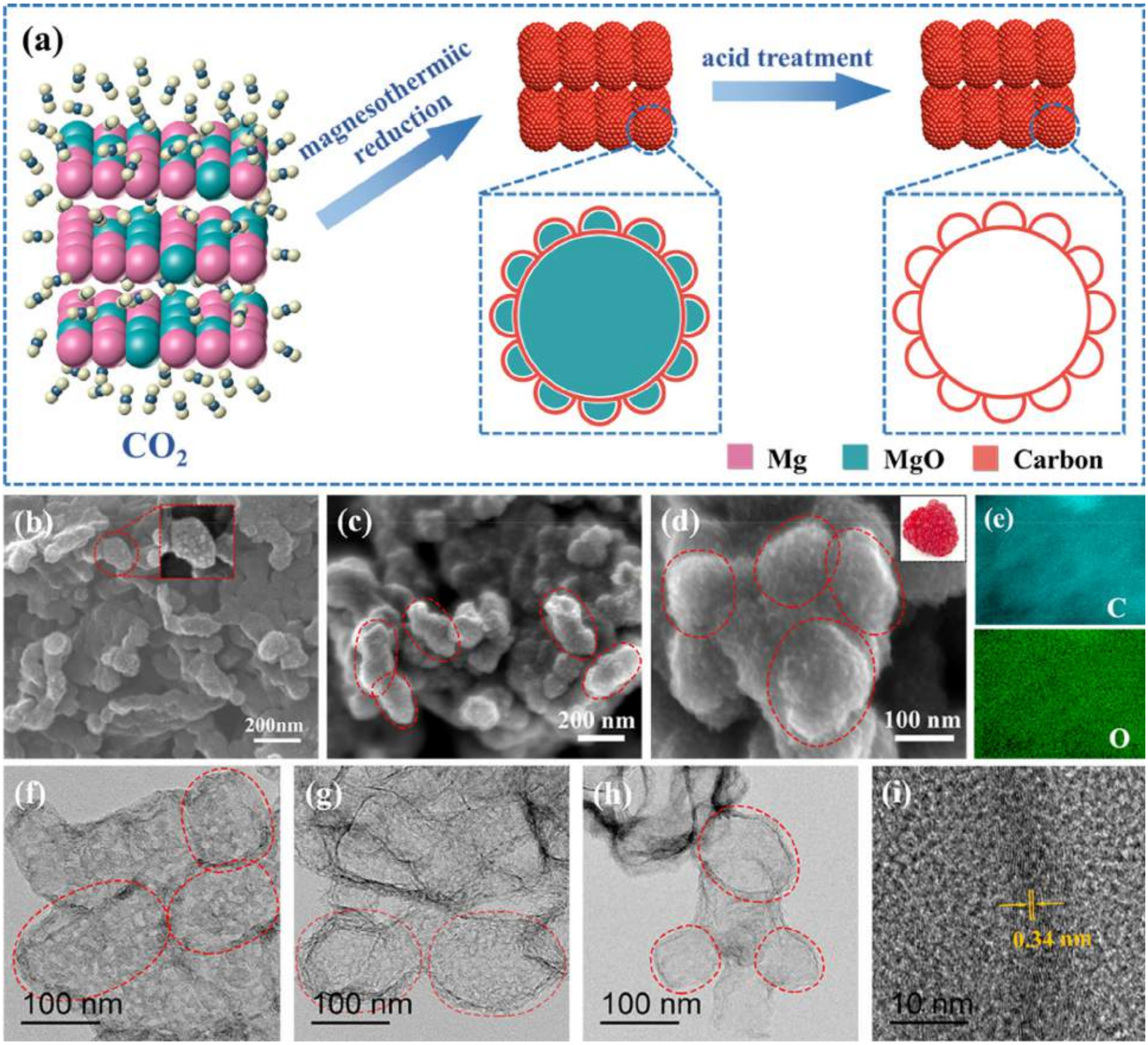

Fig. 1. Preparation and morphology of raspberry-like carbon superstructures (RCSSs). (a) Schematic illustration for the preparation of RCSSs. (b–d) SEM image of RCSSs at different magnifications. Red dashed circle indicates the single particle. It could be found that RCSSs were 100–200 nm particles with rough surfaces constructed by great number of uniformly distributed microparticles, which enabled RCSSs to exhibit a raspberry-like morphology. Every single RCSS particle contacted to each other and consequently formed carbon sheets with different orientations, well inheriting the morphology from MgO template. (e) EDS mapping images of RCSS700. TEM images of (f) RCSS700, (g) RCSS800, (h) RCSS850, and (i) HRTEM image of RCSS850.

sandwiched by two vacuum drying RCSS-based disks (8 mm in diameter, 2.5–3 mg) fully wetted by 6 M KOH aqueous solution or neat EMIMBF$_4$ ionic liquid electrolyte. The cells with EMIMBF$_4$ ionic liquid electrolyte were assembled in a glove box (Unilab Plus, Mbraun, Germany) with both contents of H_2O and $O_2 < 0.1$ ppm. Electrochemical impedance spectroscopy (EIS) and cyclic voltammetry (CV) measurement were conducted on a CHI660E electrochemical workstation (Chenhua, Shanghai, China). Galvanostatic charge/discharge (GCD) process, the cycling stability, and self-discharge tests were performed on an MSTAT4 electrochemical station (Arbin Instruments, America). Self-discharge measurement was carried out after charging the supercapacitors at a current density of 1 A g^{-1} and keeping at 1 V for 1 h.

3. Results and discussion

This bottom-up method (Fig. 1a) based on conversion of CO_2 using Mg as a reducing agent and MgO as a confined template successfully produces three-dimensional framework carbon superstructures.

$$2Mg_{(s)} + CO_{2(g)} \rightarrow 2MgO_{(s)} + C_{(s)} \tag{1}$$

Prior to the reaction between Mg and CO_2, the molten Mg gradually coated on the surface of MgO template and thus formed an MgO@Mg core-shell structure. Once CO_2 gas was introduced, the oxygen atoms in O═C═O linear molecules easily accepted the free electrons from Mg, which resulted in the deoxygenation of CO_2 and the growth of carbon skeleton [37]. Both newly generated MgO and intentionally incorporated MgO

particles acted as the template to induce continuous assembly of carbon layers and prevent the aggregation of the graphene sheets. For balancing the relationship between the decomposition of CO_2 and the precipitation of the carbon, only few graphene layers were deposited because of the templating-confined mechanism and the overlapping effect from each graphene layer [39]. Consequently, the whole hollow particles were constructed of hierarchically porous nanoparticles connected with each other, which looked like vivid raspberries (Figs. 1b–d, S1). In addition, the corresponding EDS mapping images (Fig. 1e) of RCSS700 show the uniform distribution of C and O elements. And with increasing synthesized temperature, the content of C increases while the content of O decreases from 6.07 ± 0.19% for RCSS700 to 4.74 ± 0.11% for RCSS800 and further to 3.63 ± 0.16% for RCSS850, suggesting that the higher temperature accelerates the elimination of heteroatoms (Fig. S2 and Table S1).

The raspberry-like superstructures of the various RCSS samples were further investigated by transmission electron microscopy (TEM). The TEM characterization reveals the cross-linked particles and the interconnected porous structure of raspberry-like superstructures (Figs. 1f–h and S3). Moreover, the crystallinity of the RCSSs can be easily tailored via controlling the initial reaction temperature, which increases with the increasing growth temperature. As expected, the RCSS850 exhibits much more apparent boundary as the thickness of carbon layers decreases. Under higher temperature, the sizes of the initial MgO particles and the corresponding RCSSs become larger. Simultaneously, higher temperature would accelerate the reaction and the self-generating MgO used as the templates would promote much more mesopores with smaller pore size. High-resolution TEM (HRTEM) in Fig. 1i reveals that each particle is composed of curved graphitic layers. And one typical (0 0 2) lattice plane with an interlayer spacing of 0.34 nm is indexed [29].

The intrinsic pore structure, crystallinity and structural defect of RCSSs are further characterized through surface physical measurement, XRD, and Raman spectroscopy. Nitrogen sorption isotherms of the RCSSs are plotted in Fig. 2a and the corresponding pore size distributions analyzed by DFT and BJH method are plotted in Fig. 2b and c, respectively. The SSA values are 1001, 972 and 860 $m^2\,g^{-1}$ for RCSS700, RCSS800 and RCSS850, respectively, showing a decreasing trend with the increasing temperature. All the isotherms show combined characteristics of type I and type IV isotherms according to the IUPAC classification. The sharply increasing adsorption amount at the low relative pressure implies the existence of micropores while the presence of a hysteresis loop in the P/P_0 ranging from 0.4 to 1.0 indicates the existence of mesopores. As summarized in Table S1, the micropore surface area decreases with increasing growth temperature while the mesopore surface area firstly increases from 378 to 481 $m^2\,g^{-1}$ for RCSS700, RCSS800 and then slightly decreases to 473 $m^2\,g^{-1}$ for RCSS850. This probably ascribes to the fact that a part of the micropores vanishes as the enhanced crystallization and mesopores increase in amount with a decreased pore volume from 1.07, 0.94 to 0.83 $cm^3\,g^{-1}$. XRD patterns of RCSSs are shown in Fig. 2d. Two typical diffraction peaks appear at around 25.5° and 43.3°, which are assigned to

the (0 0 2) and (1 0 0) diffraction planes [40], and the diffraction intensity is stronger with the increment of reaction temperature. In addition, the interlayer spacing of (0 0 2) crystallographic plane is calculated to be 0.34 nm, which is coincided with the HRTEM result. The intensity ratios of I_D/I_G, determined from the deconvolution of Raman spectra by four-peak fitting based on Voigt function (Figs. S4–S6), are 2.58, 1.67, and 1.58 for RCSS700, RCSS800, and RCSS850 (Fig. 2e), respectively. These values further imply fewer defects and higher crystallinity degree of the RCSSs with increasing temperature [40,41], consistent with the TEM and XRD results as-discussed above. After carefully tailoring the assembly of carbon layers and the defect intensity, the RCSS850 show high electrical conductivity of 2700 $S\,m^{-1}$ (Fig. 2f), which is higher than that of many carbon-based materials yielded from top-down or bottom-up methods [42–46]. To detect the residue of Mg and Cl elements, XPS and EDS analysis were performed. As shown in Fig. S7, a little bit of Mg (0.32%) and Cl (0.27%) elements can be found and no distinct Mg 1s peak is detected. The residual Cl element originates from the hydrochloric acid treatment. These trace residues may be ascribed to large specific surface area (~1000 $m^2\,g^{-1}$) of RCSSs, which would inevitably bond or adsorb some heteroatoms. Compared to the carbon content of 91.16% and the oxygen content of 8.25%, the remaining Mg and Cl impurities are negligible, which does not severely affect the capacitance.

The electrochemical performance of the as-prepared RCSSs in symmetric supercapacitors with 6 M KOH electrolyte is presented in Fig. 3. The obtained Nyquist plots (Fig. 3a) can be fitted into an equivalent circuit model with the combined resistance R_s, charge-transfer resistance R_{ct}, double-layer capacitance C_{dl}, and Warburg resistance (W). The combined resistance is lower than 0.5 Ω for all RCSSs from the intersection of the plots with the real axis in the high frequency region. Although the RCSS700 displays the smallest

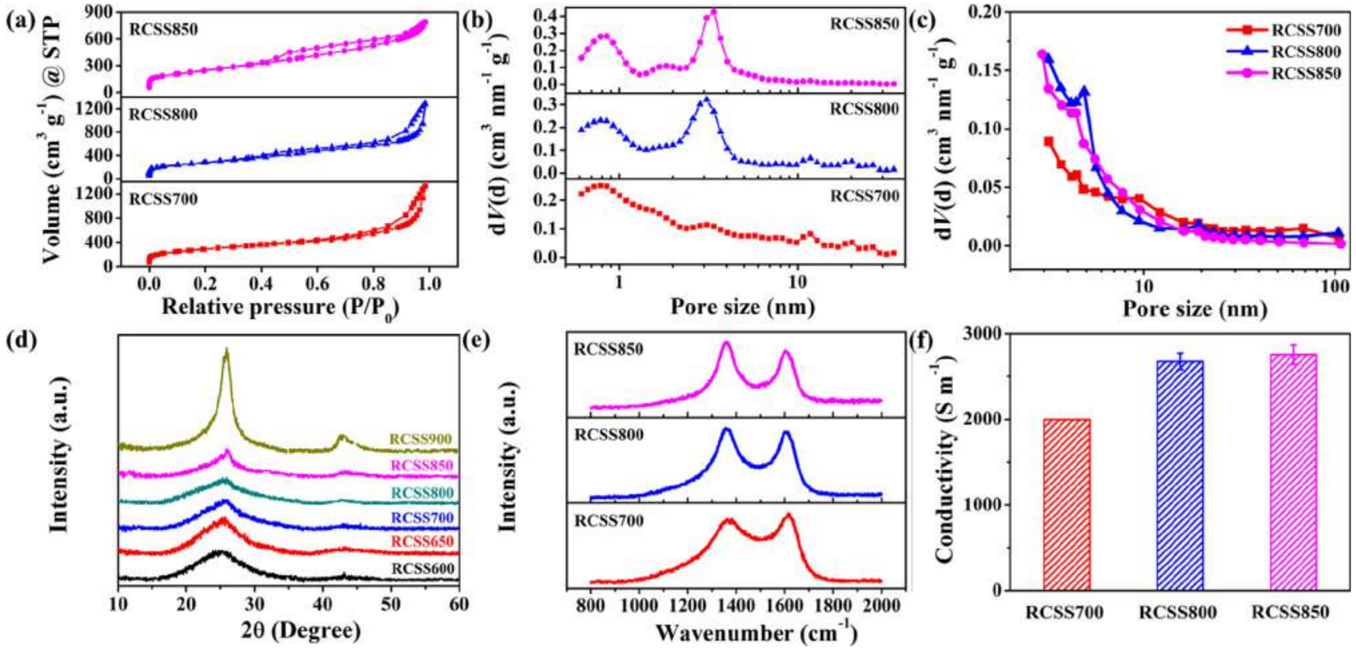

Fig. 2. Physical characterization of RCSSs. (a) N_2 adsorption/desorption isotherms of RCSSs. Pore size distribution calculated from the (b) DFT method, (c) BJH method. (d) XRD patterns. (e) Raman spectra. (f) Electrical conductivities determined by four-probe method.

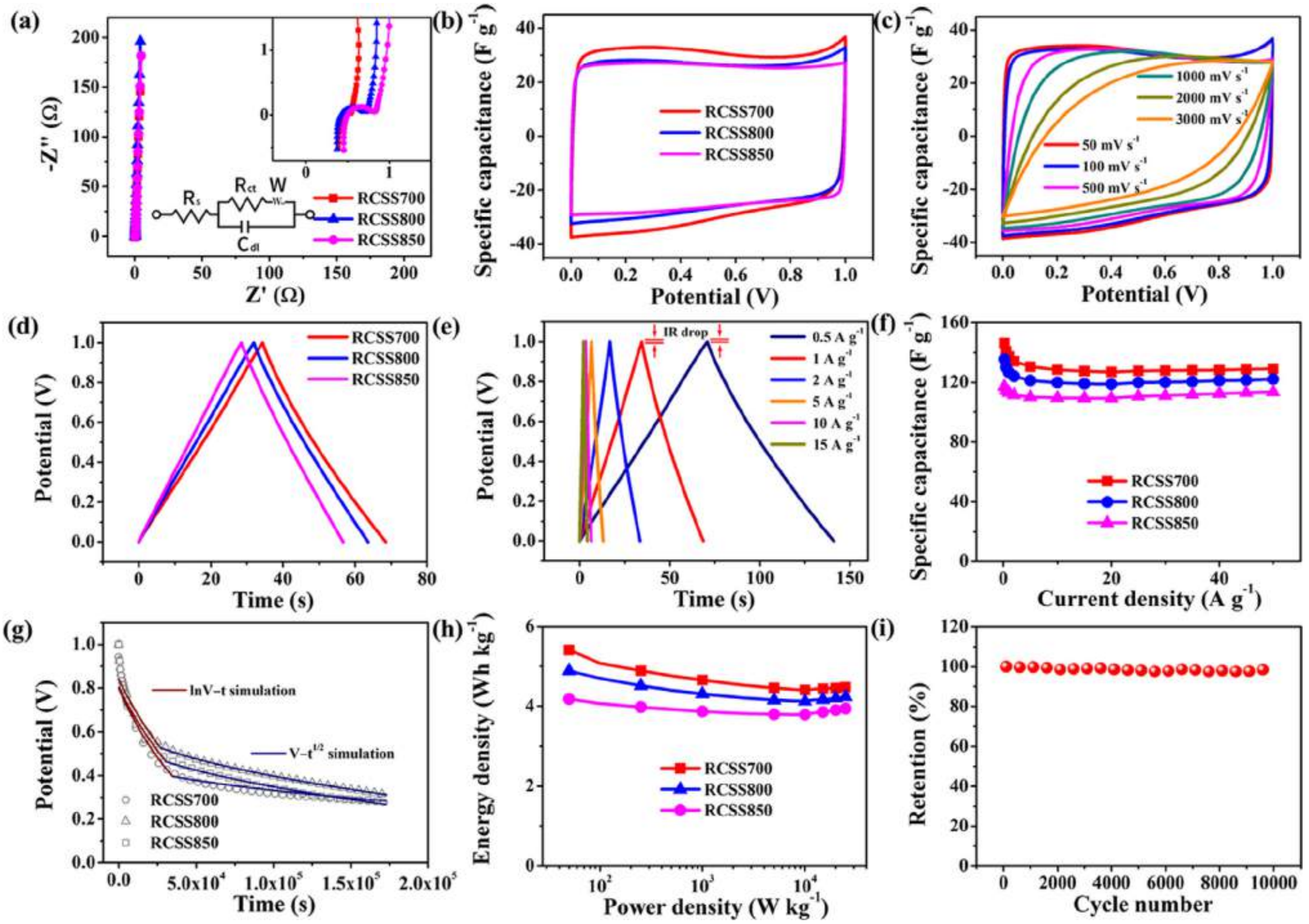

Fig. 3. Electrochemical performance of the RCSS-based symmetrical supercapacitors in 6 M KOH electrolyte. (a) Nyquist plots and the enlarged high frequency range. The inset shows the equivalent circuit diagram proposed for the analysis of EIS data. (b) CV curves for RCSSs at a scan rate of 100 mV s^{-1}. (c) CV curves of RCSS700 at different scan rates. (d) GCD curves for RCSSs at a current density of 1 A g^{-1}. (e) GCD curves of RCSS700 at different current densities. (f) Self-discharge curves and fitted results: the red lines represent the potential driving model and the blue lines follow the diffusion-controlled model. (g) The specific capacitance values at different current densities. (h) Ragone plots. (i) Cycling stability of RCSS700 at a current density of 1 A g^{-1}.

conductivity, it shows the smallest charge resistance from the EIS plots, which contributes to its much better wettability than that of RCSS800 and RCSS850 (Fig. S8). The CV curves of RCSSs exhibit rectangular shapes at a scan rate of 100 mV s^{-1} (Fig. 3b), indicating an ideal EDL capacitive behavior. Compared to the other two RCSSs, RCSS700 electrodes show the highest gravimetric capacitance, which may be owing to its highest SSA and most ion-associable pores.

The CV curves of RCSS700 from 50 to 3000 mV s^{-1} are presented in Fig. 3c. Even though the scan rate greatly increases to 1000 mV s^{-1}, the CV curve of RCSS700 still maintains a good rectangular shape, indicating good rate-capability. The RCSS800 and RCSS850 also show nearly ideal rectangular shape at both low and very high scan rate (Fig. S9). The galvanostatic charge/discharge (GCD) curves of RCSSs at 1 A g^{-1} are in perfect isosceles triangle shape shown in Fig. 3d (the GCD curves of RCSSs at different current densities are also plotted, SI, Fig. S10). Typical GCD curves at high current densities for the RCSS700 show negligible IR drop (Figs. 3e and S15), demonstrating its small R_s. The specific capacitances of RCSS700 electrodes are 146.2 F g^{-1} at 0.2 A g^{-1} and 129.1 F g^{-1} at a high current density of 50 A g^{-1}, showing a capacitance retention of 88.3% (Fig. 3f). The slightly increase in specific capacitance could be ascribed to the a little bit lower discharge capacitance at high work voltage than that at low work voltage (Fig. S11).

Fig. 3g displays the self-discharge behavior of RCSS-based supercapacitors. In order to understand the self-discharge mechanism, the curves are fitted by a dual-mechanism (DM) model, which can be divided into two parts. The red curves represent the fitting from the potential driving model ($\ln V \propto t$) and the blue curves follow the diffusion-control model ($V \propto t^{1/2}$) [47,48]. When the potential field acts as the dominating driving force, the self-discharge rate of RCSS700 is much faster than that of RCSS800 and RCSS850. It takes 5.84 h for RCSS700 to drop from its initial voltage (1 V) to 0.5 V. By comparison, it takes 11.0 h for RCSS800 and 7.39 h for RCSS850. This is because RCSS700 possesses the highest oxygen functional groups as indicated by EDS analysis that causes a faster faradaic reaction during the first stage, resulting in the fastest self-discharge at potential driving stage [49–51]. On the other hand, the self-discharge rate becomes the slowest for RCSS700 electrodes at the second stage. This is because the RCSS700 sample possesses the largest pore volume that promotes the charge penetration into the deep of the pores and hence alleviates the charge redistribution process [52,53].

Ragone plots in Fig. 3h demonstrate that RCSS700 can deliver a maximum energy density of 5.1 Wh kg^{-1} at a power density of 0.1 kW kg^{-1}. And the energy density decreases to 4.5 Wh kg^{-1} at 2.5 kW kg^{-1}. Moreover, the RCSS700 displays a high capacitance retention of 98.3% after 10,000 cycles at a current density of 1 A g^{-1} (Fig. 3i), revealing remarkable cycling stability.

To further investigate the electrochemical properties of RCSSs, two electrode symmetric supercapacitors based on RCSSs electrode were assembled in neat $EMIMBF_4$. Careful evaluation demonstrated the

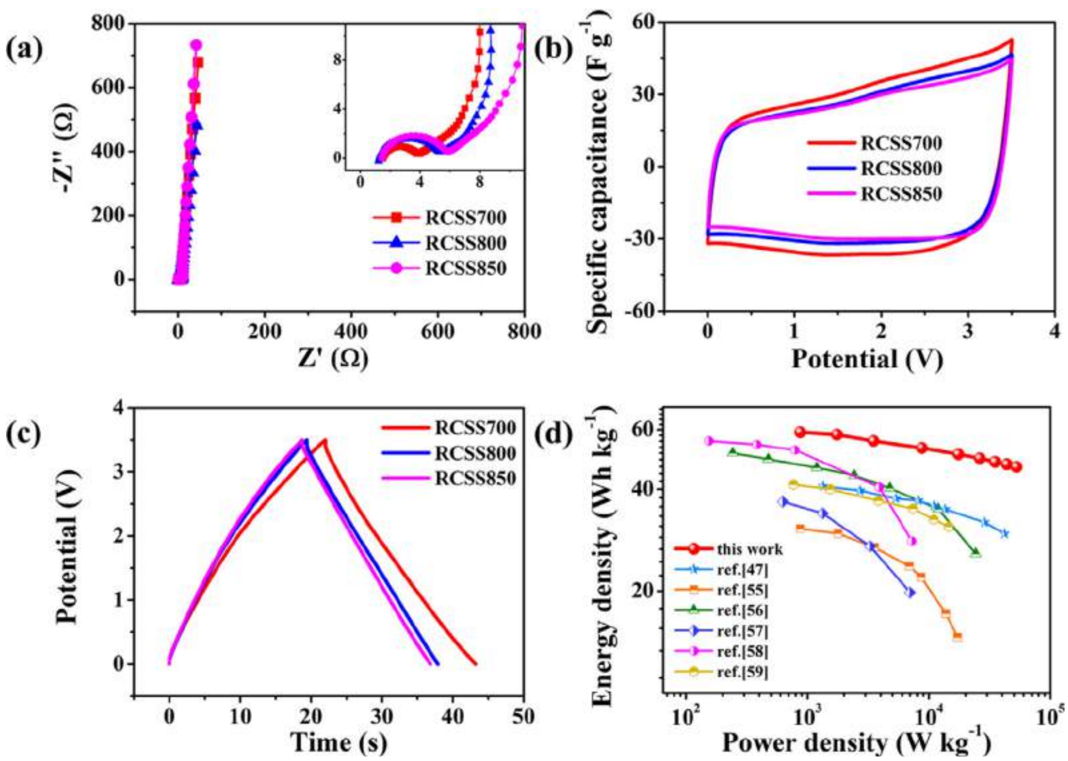

Fig. 4. Electrochemical performance of the RCSS-based symmetrical supercapacitors in $EMIMBF_4$ ionic liquid electrolyte. (a) Nyquist plots and the inset magnifies the high-frequency range. (b) CV curves for RCSSs at a scan rate of 100 mV s^{-1}. (c) GCD curves for RCSSs at a current density of 5 A g^{-1}. (d) Ragone plots of RCSS700 in comparison with other carbon materials in $EMIMBF_4$ ionic liquid electrolytes.

voltage window could be up to 3.5 V for RCSS-based supercapacitors in $EMIMBF_4$ ionic liquid electrolyte (Fig. S12). As shown in Fig. 4a, the RCSS700 shows the smallest charge resistance from the EIS plots. And considering that the ionic liquid is easy to absorb moisture in atmospheric environment, we do not perform contact angle test for $EMIMBF_4$. As in $EMIMBF_4$ ionic liquid electrolyte, we assum that the ion transport rate became the main parameter to affect the charge transfer resistance. Because RCSS700 shows larger average mesopore volume (1.07 cm^3 g^{-1}), than that of RCSS850 (0.83 cm^3 g^{-1}) and RCSS800 (0.94 cm^3 g^{-1}), electrolyte ions penetrate much easier into the RCSS700 to

form a double layer capacitive, which reduces the impedance [54]. The nearly ideal rectangular CV curves for RCSS-based supercapacitors with neat $EMIMBF_4$ at 100 mV s^{-1} (Fig. 4b) and various scan rates (Fig. S13) again imply that electrostatic attraction occurs at the electrode-electrolyte interface and the existence of ideal EDL capacitive behavior. Figs. 4c and S4 show the GCD curves at different current densities. The specific capacitance at 0.5 A g^{-1} is 138.8 F g^{-1} and maintains 109.3 F g^{-1} at 30 A g^{-1}. This value is comparable to that of the RCSS-based supercapacitors in 6 M KOH electrolyte. The abundant mesopores in RCSSs can not only contribute to the formation of EDL capacitance but also provide a facile path for penetration and transportation of electrolyte ions, which is especially critical for ionic liquid. On the other hand, the ionic liquid electrolyte supplies a wide work voltage, which is more favorable for high specific capacitance of RCSSs (Fig. S16). When the current density increases by 60 times, 79% of the capacitance is remained. In addition, the initial capacitance value of 83.5% is retained after 10,000 cycles at 1 A g^{-1} (Fig. S17).

The Ragone plots in Fig. 4d compare the energy and power characteristics of the RCSSs. The maximum energy density of the RCSS700-based supercapacitor is 59.0 Wh kg^{-1} at a power density of 875 W kg^{-1}. The high rate-capability of RCSSs leads to a high energy density of 46.5 Wh kg^{-1} even at high power density of 52.5 kW kg^{-1}, which is superior to many carbon-based electrodes (Fig. 4d) [47,55–59]. In addition, a detailed comparison of the RCSSs with other carbon-based electrodes for supercapacitors in ionic liquid electrolytes has been listed in Table S2.

The fascinating results of electrochemical performance demonstrate that the rationally designed raspberry-like carbon superstructures possess high rate-capability, long-term cyclic stability and high energy density along with high power density. The remarkable electrochemical performance can be attributed to the critical features of well-organized porous structure, high accessible surface area, and interconnected framework. On one hand, the presence of abundant mesopores not only offer high accessible surface area and active sites for charge storage, but also promote the migration of electrolyte ions, through providing free access for electrolyte ions into the micropores [7,60–63]. This will result in high capacitance and is true for RCSS-700 electrodes. On the other hand, the crystallized carbon framework enables good electrical conductivity for RCSSs, and hence contribute to small charge transfer resistance, which is critical to high rate-capability [38,42,61–63]. In short, high electrical conductivity and fined-tuned pore structure of raspberry-like carbon superstructures makes them as good candidates in advanced supercapacitors.

4. Conclusion

In conclusion, we have demonstrated that CO_2 can be converted into raspberry-like carbon superstructures with high accessible SSA and high electrical conductivity (up to 2700 S m^{-1}). In-situ transformed carbon layers self-assemble on well-dispersed MgO templating particles, resulting in interconnected pore structure, which is crucial to fast ion transfer and rapid electric double layer capacitive establishment. RCSS-based supercapacitors deliver a high energy density of 46.5 Wh kg^{-1} at a high power density of 52.5 kW kg^{-1} in ionic liquid electrolyte. Notably, the devices show > 98% capacitance retention after 10,000 cycles at 1 A g^{-1} in 6 M KOH electrolyte, demonstrating excellent cycling stability. Herein reported promising results unambiguously demonstrate that the rationally designed carbon superstructures based on self-assembled strategy have great potential in application for advanced supercapacitors and also other devices such as the batteries, fuel cells, and devices for hydrogen generation.

Acknowledgements

We are thankful to Southwest Jiaotong University Analytical and Testing Center for the SEM measurements. This work is supported by the National Natural Science Foundation of China(No. 51602265), the Special Funding of China Postdoctoral Science Foundation (No. 2018T110992), the Sichuan Science and Technology Program (No. 2018RZ0074) as well as the Cultivation Program for the Excellent Doctoral Dissertation of Southwest Jiaotong University (No. D-YB201709).

Appendix A. Supplementary data

Supplementary data to this article can be found online at https://doi.org/10.1016/j.cej.2019.01.007.

References

[1] J.R. Mille, P. Simon, Electrochemical capacitors for energy management, Science 321 (2008) 651–652, https://doi.org/10.1126/science.1158736.

[2] W. Gu, G. Yushin, Review of nanostructured carbon materials for electrochemical capacitor applications: advantages and limitations of activated carbon, carbide-derived carbon, zeolite-templated carbon, carbon aerogels, carbon nanotubes, onion-like carbon, and graphene, Wiley Interdiscip. Rev.: Energy Environ. 3 (2014) 424–473, https://doi.org/10.1002/wene.102.

[3] B. Gao, X. Li, K. Ding, C. Huang, Q. Li, P.K. Chu, K. Huo, Recent progress in nanostructured transition metal nitrides for advanced electrochemical energy storage, J. Mater. Chem. A (2018), https://doi.org/10.1039/c8ta05760e.

[4] P. Qin, X. Li, B. Gao, J. Fu, L. Xia, X. Zhang, K. Huo, W. Shen, P.K. Chu, Hierarchical TiN nanoparticles-assembled nanopillars for flexible supercapacitors with high volumetric capacitance, Nanoscale 10 (2018) 8728–8734, https://doi.org/10.1039/c8nr01485j.

[5] H. Song, J. Fu, K. Ding, C. Huang, K. Wu, X. Zhang, B. Gao, K. Huo, X. Peng, P.K. Chu, Flexible Nb$_2$O$_5$ nanowires/graphene film electrode for high-performance hybrid Li-ion supercapacitors, J. Power Sources 328 (2016) 599–606, https://doi.org/10.1016/j.jpowsour.2016.08.052.

[6] F. Beguin, V. Presser, A. Balducci, E. Frackowiak, Carbons and electrolytes for advanced supercapacitors, Adv. Mater. 26 (2014) 2219–2251, https://doi.org/10.1002/adma.201304137.

[7] Z. Chen, K. Liu, S. Liu, L. Xia, J. Fu, X. Zhang, C. Zhang, B. Gao, Porous active carbon layer modified graphene for high-performance supercapacitor, Electrochim. Acta 237 (2017) 102–108, https://doi.org/10.1016/j.electacta.2017.03.177.

[8] X. Chu, H. Zhang, H. Su, F. Liu, B. Gu, H. Huang, H. Zhang, W. Deng, X. Zheng, W. Yang, A novel stretchable supercapacitor electrode with high linear capacitance, Chem. Eng. J. 349 (2018) 168–175, https://doi.org/10.1016/j.cej.2018.05.090.

[9] H. Su, H. Huang, H. Zhang, X. Chu, B. Zhang, B. Gu, X. Zheng, S. Wu, W. He, C. Yan, J. Chen, W. Yang, In situ direct method to massively prepare hydrophilic porous carbide-derived carbons for high-performance supercapacitors, ACS Appl. Energy Mater. 1 (2018) 3544–3553, https://doi.org/10.1021/acsaem.8b00764.

[10] Q. Meng, K. Qin, L. Ma, C. He, E. Liu, F. He, C. Shi, Q. Li, J. Li, N. Zhao, N-doped porous carbon nanofibers/porous silver network hybrid for high-rate supercapacitor electrode, ACS Appl. Mater. Interfaces 9 (2017) 30832–30839, https://doi.org/10.1021/acsami.7b08610.

[11] H. Jiang, P.S. Lee, C. Li, 3D carbon based nanostructures for advanced supercapacitors, Energy Environ. Sci. 6 (2013) 41–53, https://doi.org/10.1039/c2ee23284g.

[12] Y. Cao, V. Fatemi, S. Fang, K. Watanabe, T. Taniguchi, E. Kaxiras, P. Jarillo-Herrero, Unconventional superconductivity in magic-angle graphene superlattices, Nature 556 (2018) 43–50, https://doi.org/10.1038/nature26160.

[13] G.Q. Xin, T.K. Yao, H.T. Sun, S.M. Scott, D.L. Shao, G.K. Wang, J. Lian, Highly thermally conductive and mechanically strong graphene fibers, Science 349 (2015) 1083–1087, https://doi.org/10.1126/science.aaa6502.

[14] G. Wan, M. Ma, A. Jia, L. Chen, Y. Chen, X. Cui, H. Chen, J. Shi, A 3D hierarchical assembly of optimized heterogeneous carbon nanosheets for highly efficient electrocatalysis, J. Mater. Chem. A 4 (2016) 11625–11629, https://doi.org/10.1039/c6ta03930h.

[15] S. Xiong, J. Fan, Y. Wang, J. Zhu, J. Yu, Z. Hu, A facile template approach to nitrogen-doped hierarchical porous carbon nanospheres from polydopamine for high-performance supercapacitors, J. Mater. Chem. A 5 (2017) 18242–18252, https://doi.org/10.1039/c7ta05880b.

[16] T. Chen, B. Cheng, G. Zhu, R. Chen, Y. Hu, L. Ma, H. Lv, Y. Wang, J. Liang, Z. Tie, Z. Jin, J. Liu, Highly efficient retention of polysulfides in “sea urchin”-like carbon nanotube/nanopolyhedra superstructures as cathode material for ultralong-life lithium-sulfur batteries, Nano Lett. 17 (2017) 437–444, https://doi.org/10.1021/acs.nanolett.6b04433.

[17] Z. Xu, X. Zhuang, C. Yang, J. Cao, Z. Yao, Y. Tang, J. Jiang, D. Wu, X. Feng, Nitrogen-doped porous carbon superstructures derived from hierarchical assembly of polyimide nanosheets, Adv. Mater. 28 (2016) 1981–1987, https://doi.org/10.1002/adma.201505131.

[18] H. Cheng, Y. Hu, F. Zhao, Z. Dong, Y. Wang, N. Chen, Z. Zhang, L. Qu, Moisture-activated torsional graphene-fiber motor, Adv. Mater. 26 (2014) 2909–2913, https://doi.org/10.1002/adma.201305708.

[19] G. Tao, J. Wang, Gold nanorod@nanoparticle seed-SERS nanotags/graphene oxide plasmonic superstructured nanocomposities as an “on-off” SERS aptasensor, Carbon 133 (2018) 209–217, https://doi.org/10.1016/j.carbon.2018.03.037.

[20] M.A. Worsley, P.J. Pauzauskie, T.Y. Olson, J. Biener, J.H. Satcher, T.F. Baumann, Synthesis of graphene aerogel with high electrical conductivity, J. Am. Chem. Soc. 132 (2010) 14067–14069, https://doi.org/10.1021/ja1072299.

[21] L. Wang, H.K. Bisoyi, Z. Zheng, K.G. Gutierrez-Cuevas, G. Singh, S. Kumar, T.J. Bunning, Q. Li, Stimuli-directed self-organized chiral superstructures for adaptive windows enabled by mesogen-functionalized graphene, Mater. Today 20 (2017) 230–237, https://doi.org/10.1016/j.mattod.2017.04.028.

[22] Y. Chen, X. Zhang, D. Zhang, P. Yu, Y. Ma, High performance supercapacitors based on reduced graphene oxide in aqueous and ionic liquid electrolytes, Carbon 49 (2011) 573–580, https://doi.org/10.1016/j.carbon.2010.09.060.

[23] Y. Wang, W. Lai, N. Wang, Z. Jiang, X. Wang, P. Zou, Z. Lin, H.J. Fan, F. Kang, C.P. Wong, C. Yang, A reduced graphene oxide/mixed-valence manganese oxide composite electrode for tailorable and surface mountable supercapacitors with high capacitance and super-long life, Energy Environ. Sci. 10 (2017) 941–949, https://doi.org/10.1039/c6ee03773a.

[24] S. Ye, J. Feng, Self-assembled three-dimensional hierarchical graphene/polypyrrole nanotube hybrid aerogel and its application for supercapacitors, ACS Appl. Mater. Interfaces 6 (2014) 9671–9679, https://doi.org/10.1021/am502077p.

[25] B. Han, E. Zhang, G. Cheng, L. Zhang, D. Wang, X. Wang, Hydrothermal carbon superstructures enriched with carboxyl groups for highly efficient uranium removal, Chem. Eng. J. 338 (2018) 734–744, https://doi.org/10.1016/j.cej.2018.01.089.

[26] S. Chen, D.M. Koshy, Y. Tsao, R. Pfattner, X. Yan, D. Feng, Z. Bao, Highly tunable and facile synthesis of uniform carbon flower particles, J. Am. Chem. Soc. 140 (2018) 10297–10304, https://doi.org/10.1021/jacs.8b05825.

[27] J. Liang, S. Chen, M. Xie, Y. Wang, X. Guo, X. Guo, W. Ding, Expeditious fabrication of flower-like hierarchical mesoporous carbon superstructures as supercapacitor electrode materials, J. Mater. Chem. A 2 (2014) 16884–16891, https://doi.org/10.1039/c4ta03209h.

[28] W.J. Ong, L.L. Tan, S.P. Chai, S.T. Yong, Graphene oxide as a structure-directing agent for the two-dimensional interface engineering of sandwich-like graphene-g-C$_3$N$_4$ hybrid nanostructures with enhanced visible-light photoreduction of CO$_2$ to methane, Chem. Commun. 51 (2015) 858–861, https://doi.org/10.1039/c4cc08996k.

[29] D.A. Torelli, S.A. Francis, J.C. Crompton, A. Javier, J.R. Thompson, B.S. Brunschwig, M.P. Soriaga, N.S. Lewis, Nickel-gallium-catalyzed electrochemical reduction of co$_2$ to highly reduced products at low overpotentials, ACS Catal. 6 (2016) 2100–2104, https://doi.org/10.1021/acscatal.5b02888.

[30] Z. Weng, J. Jiang, Y. Wu, Z. Wu, X. Guo, K.L. Materna, W. Liu, V.S. Batista, G.W. Brudvig, H. Wang, Electrochemical CO$_2$ reduction to hydrocarbons on a heterogeneous molecular cu catalyst in aqueous solution, J. Am. Chem. Soc. 138 (2016) 8076–8079, https://doi.org/10.1021/jacs.6b04746.

[31] J. Yu, J. Jin, B. Cheng, M. Jaroniec, A noble metal-free reduced graphene oxide-CdS nanorod composite for the enhanced visible-light photocatalytic reduction of CO$_2$ to solar fuel, J. Am. Chem. Soc. 2 (2014) 3407, https://doi.org/10.1039/c3ta14493c.

[32] F. Studt, I. Sharafutdinov, F. Abild-Pedersen, C.F. Elkjaer, J.S. Hummelshoj, S. Dahl, I. Chorkendorff, J.K. Norskov, Discovery of a Ni-Ga catalyst for carbon dioxide reduction to methanol, Nat. Chem. 6 (2014) 320–324, https://doi.org/10.1038/nchem.1873.

[33] O. Martin, A.J. Martin, C. Mondelli, S. Mitchell, T.F. Segawa, R. Hauert, C. Drouilly, D. Curulla-Ferre, J. Perez-Ramirez, Indium oxide as a superior catalyst for methanol synthesis by CO$_2$ hydrogenation, Angew. Chem. 55 (2016) 6261–6265, https://doi.org/10.1002/anie.201600943.

[34] S. Back, H. Kim, Y. Jung, Selective heterogeneous CO$_2$ electroreduction to methanol, ACS Catal. 5 (2015) 965–971, https://doi.org/10.1021/cs501600x.

[35] W. Wei, K. Sun, Y.H. Hu, Synthesis of 3D cauliflower-fungus-like graphene from CO$_2$ as a highly efficient counter electrode material for dye-sensitized solar cells, J. Mater. Chem. A 2 (2014) 16842–16846, https://doi.org/10.1039/c4ta03909b.

[36] Z. Xing, B. Wang, W. Gao, C. Pan, J.K. Halsted, E.S. Chong, J. Lu, X. Wang, W. Luo, C.H. Chang, Y. Wen, S. Ma, K. Amine, X. Ji, Reducing CO$_2$ to dense nanoporous graphene by Mg/Zn for high power electrochemical capacitors, Nano Energy 11 (2015) 600–610, https://doi.org/10.1016/j.nanoen.2014.11.011.

[37] H. Zhang, X. Zhang, X. Sun, Y. Ma, Shape-controlled synthesis of nanocarbons through direct conversion of carbon dioxide, Sci. Rep. 3 (2013) 3534, https://doi.org/10.1038/srep03534.

[38] C. Li, X. Zhang, K. Wang, X. Sun, G. Liu, J. Li, H. Tian, J. Li, Y. Ma, Scalable self-propagating high-temperature synthesis of graphene for supercapacitors with superior power density and cyclic stability, Adv. Mater. 29 (2017) 1604690, https://doi.org/10.1002/adma. 2014.11.011.

[39] M.H. Ruemmeli, C. Kramberger, A. Grueneis, P. Ayala, T. Gemming, B. Buechner, T. Pichler, On the graphitization nature of oxides for the formation of carbon nanostructures, Chem. Mater. 19 (2007) 4105–4107, https://doi.org/10.1021/cm0712220.

[40] J. Guo, H. Guo, L. Zhang, B. Yang, J. Cui, Hierarchically porous carbon as a high-rate and long-life electrode material for high-performance supercapacitors,

ChemElectroChem 5 (2018) 770–777, https://doi.org/10.1002/celc.201701286.

[41] T. Purkait, G. Singh, M. Singh, D. Kumar, R.S. Dey, Large area few-layer graphene with scalable preparation from waste biomass for high-performance supercapacitor, Sci. Rep. 7 (2017) 15239, https://doi.org/10.1038/s41598-017-15463-w.

[42] W. Yang, L. Hou, X. Xu, Z. Li, X. Ma, F. Yang, Y. Li, Carbon nitride template-directed fabrication of nitrogen-rich porous graphene-like carbon for high performance supercapacitors, Carbon 130 (2018) 325–332, https://doi.org/10.1016/j.carbon.2018.01.032.

[43] J. Zhu, Y. Xu, Y. Zhang, T. Feng, J. Wang, S. Mao, L. Xiong, Porous and high electronic conductivity nitrogen-doped nano-sheet carbon derived from polypyrrole for high-power supercapacitors, Carbon 107 (2016) 638–645, https://doi.org/10.1016/j.carbon.2016.06.063.

[44] L. Zhang, T. You, T. Zhou, X. Zhou, F. Xu, Interconnected hierarchical porous carbon from lignin-derived byproducts of bioethanol production for ultra-high performance supercapacitors, ACS Appl. Mater. Interfaces 8 (2016) 13918–13925, https://doi.org/10.1021/acsami.6b02774.

[45] R. Shao, J. Niu, J. Liang, M. Liu, Z. Zhang, M. Dou, Y. Huang, F. Wang, Mesopore- and macropore-dominant nitrogen-doped hierarchically porous carbons for high-energy and ultrafast supercapacitors in non-aqueous electrolytes, ACS Appl. Mater. Interfaces 9 (2017) 42797–42805, https://doi.org/10.1021/acsami.7b14390.

[46] W. Tian, Q. Gao, L. Zhang, C. Yang, Z. Li, Y. Tan, W. Qian, H. Zhang, Renewable graphene-like nitrogen-doped carbon nanosheets as supercapacitor electrodes with integrated high energy-power properties, J. Mater. Chem. A 4 (2016) 8690–8699, https://doi.org/10.1039/c6ta02828d.

[47] Q. Zhang, J. Rong, D. Mab, B. Wei, The governing self-discharge processes in activated carbon fabric-based supercapacitors with different organic electrolytes, Energy Environ. Sci. 4 (2011) 2152–2159, https://doi.org/10.1039/c0ee00773k.

[48] A. Lewandowski, P. Jakobczyk, M. Galinski, M. Biegun, Self-discharge of electrochemical double layer capacitors, PCCP 15 (2013) 8692–8699, https://doi.org/10.1039/c3cp44612c.

[49] B.E. Conway, W.G. Pell, T.C. Li, Diagnostic analyses for mechanisms of self-discharge of electrochemical capacitors and batteries, J. Power Sources 65 (1997) 53–59, https://doi.org/10.1016/S0378-7753(97)02468-3.

[50] I.S. Ike, I. Sigalas, S. Iyuke, Understanding performance limitation and suppression of leakage current or self-discharge in electrochemical capacitors: a review, Phys. Chem. Chem. Phys. 18 (2015) 661–680, https://doi.org/10.1039/c5cp05459a.

[51] J. Niu, W.G. Pell, B.E. Conway, Requirements for performance characterization of C double-layer supercapacitors: applications to a high specific-area C-cloth material, J. Power Sources 156 (2006) 725–740, https://doi.org/10.1016/j.jpowsour.2005.06.002.

[52] M.A. Davis, H.A. Andreas, Identification and isolation of carbon oxidation and charge redistribution as self-discharge mechanisms in reduced graphene oxide electrochemical capacitor electrodes, Carbon 139 (2018) 299–308, https://doi.org/10.1016/j.carbon.2018.06.065.

[53] C. Hao, X. Wang, Y. Yin, Z. You, Analysis of charge redistribution during self-discharge of double-layer supercapacitors, J. Electron. Mater. 45 (2016) 2160–2171, https://doi.org/10.1007/s11664-016-4357-0.

[54] J. Lee, R. Nankya, A. Kim, H. Jung, Fine-tuning the pore size of mesoporous graphene in a few nanometer-scale by controlling the interaction between graphite oxide sheets, Electrochim. Acta 290 (2018) 496–505, https://doi.org/10.1016/j.electacta.2018.09.110.

[55] H. Zhang, X. Zhang, X. Sun, D. Zhang, H. Lin, C. Wang, H. Wang, Y. Ma, Large-scale production of nanographene sheets with a controlled mesoporous architecture as high-performance electrochemical electrode materials, ChemSusChem 6 (2013) 1084–1090, https://doi.org/10.1002/cssc.201200904.

[56] L. Lu, W. Li, L. Zhou, Y. Zhang, Z. Zhang, Y. Chen, J. Liu, L. Liu, W. Chen, Y. Zhang, Impact of size on energy storage performance of graphene based supercapacitor electrode, Electrochim. Acta 219 (2016) 463–469, https://doi.org/10.1016/j.electacta.2016.10.020.

[57] X. Wang, C. Lu, H. Peng, X. Zhang, Z. Wang, G. Wang, Efficiently dense hierarchical graphene based aerogel electrode for supercapacitors, J. Power Sources 324 (2016) 188–198, https://doi.org/10.1016/j.jpowsour.2016.05.085.

[58] M. Sevilla, G.A. Ferrero, N. Diez, A.B. Fuertes, One-step synthesis of ultra-high surface area nanoporous carbons and their application for electrochemical energy storage, Carbon 131 (2018) 193–200, https://doi.org/10.1016/j.carbon.2018.02.021.

[59] Y. Cui, H. Wang, N. Mao, W. Yu, J. Shi, M. Huang, W. Liu, S. Chen, X. Wang, Tuning the morphology and structure of nanocarbons with activating agents for ultrafast ionic liquid-based supercapacitors, J. Power Sources 361 (2017) 182–194, https://doi.org/10.1016/j.jpowsour.2017.06.087.52.

[60] K.S. Lakhi, D.H. Park, K. Al-Bahily, W. Cha, B. Viswanathan, J.H. Choy, A. Vinu, Mesoporous carbon nitrides: synthesis, functionalization, and applications, Chem. Soc. Rev. 46 (2017) 72–101, https://doi.org/10.1039/c6cs00532b.

[61] Y. Wang, Y. Song, Y. Xia, Electrochemical capacitors: mechanism, materials, systems, characterization and applications, Chem. Soc. Rev. 45 (2016) 5925–5950, https://doi.org/10.1039/c5cs00580a.

[62] Q. Wang, J. Yan, Z. Fan, Carbon materials for high volumetric performance supercapacitors: design, progress, challenges and opportunities, Energy Environ. Sci. 9 (2016) 729–762, https://doi.org/10.1039/c5ee03109e.

[63] H. Su, H. Zhang, F. Liu, F. Chun, B. Zhang, X. Chu, H. Huang, W. Deng, B. Gu, H. Zhang, X. Zheng, M. Zhu, W. Yang, High power supercapacitors based on hierarchically porous sheet-like nanocarbons with ionic liquid electrolytes, Chem. Eng. J. 322 (2017) 73–81, https://doi.org/10.1016/j.cej.2017.04.012.